

# Complicated reflection of linear internal tides from the Tasman continental slope

JODY M. KLYMAK, \*

*The University of Victoria, Victoria, Canada*

Harper L. Simmons and Dmitry Braznikov

*Affiliation, City, State/Province, Country*

Samuel Kelly

*Affiliation, City, State/Province, Country*

Jennifer A. MacKinnon, Matthew H. Alford, and Robert Pinkel

*Affiliation, City, State/Province, Country*

Jonathan D. Nash

*Affiliation, City, State/Province, Country*

---

\* Corresponding author address: Jody Klymak, University of Victoria, Victoria, BC, Canada

E-mail: jklymak@uvic.ca

## ABSTRACT

The reflection of a low-mode incident internal tide on the Tasman continental slope is investigated using simulations of both the real topography, and simplified topographies. The majority of the slope is super-critical to the internal tide, but the response to the slope is complicated by a number of factors. The incoming beam is confined in space, it impacts the slope at an angle, there is a roughly cylindrical rise directly offshore of the slope, and a slope-mode wave is excited. These effects are isolated in simulations that significantly simplify the topography. Determining a reflected signal from an incident one is non-trivial, even in a numerical model, and the technique used here is to remove the reflector from the simulation and subtract an incident response from the total response to arrive at a reflected signal. Overall, the real slope reflects approximately 65% of the mode-1 internal tide as a mode-1 signal, which is less than two-dimensional linear calculations would predict, likely due to three-dimensional concavity of the topography. A synthetic three-point mooring array can predict almost any reflectivity because of spatial inhomogeneity. The Tasman Rise serves to diffract the incoming tidal beam into two beams, one focused downstream, and one diffracted to the north, with a substantial null in incoming energy between them. Along-slope heterogeneity is further enhanced by a partially trapped super-inertial slope wave that propagates along the continental slope, removing energy from the internal tide in some spots and re-radiating it further north. This wave is present even in a simplified straight-shelf topography.

# 1. Introduction

Energy is lost from the surface tide when it interacts with topography, and in the deep ocean is largely redistributed as an internal tide. The fate of the internal tide is unclear, but surely depends on the dominant wavelengths that are forced. Gentle topography that is subcritical to the internal tide is likely dominated by higher vertical modes and is thought to break via wave-wave interactions relatively close to the topography (i.e. Polzin 2009; St. Laurent and Garrett 2002). However, steeper supercritical topography, while exhibiting significant local dissipation, tends to radiate a large fraction of the internal tide away from the topography as low-mode waves (i.e. at Hawaii Klymak et al. 2006; Carter et al. 2008). Given that a significant fraction of the internal tide energy is generated at steep topography (Legg and Klymak 2008), and that the distribution of the mixing it eventually drives has impacts on understanding the distribution of ocean properties and the strength of the overturning circulation (i.e. Melet et al. 2013), it is desirable to understand where and how this energy breaks.

One candidate sink for the low-mode internal tide is reflection and scattering from continental slopes. These slopes are known to be hotspots of turbulent mixing from the few observational studies to date (Nash et al. 2007; Klymak et al. 2011; Martini et al. 2013). However, these studies have also demonstrated some of the difficulties in tracking internal tide energy on these slopes. Net internal-tide fluxes are relatively straight forward to measure, but ideally we would like to separate the incident and reflected fluxes if a parameterization of turbulence on the slope is to be made since the incident fluxes are what drive the turbulence. The reflectivity of a continental slope is basically the ratio of the energy flux convergence divided by the total incident flux:

$$r = \frac{F_{in} - F_{out}}{F_{in}},$$

where  $F$  is depth integrated for a two-dimensional budget or line-integrated for a three-dimensional one. Even simple two-dimensional linear models of reflection indicate that determining the reflectivity will be challenging, with reflection co-efficients strongly depending on the modal content and phases of the incident internal tides (Klymak et al. 2011) and the local surface tide (Kelly and Nash 2010). These linear models have been used globally to estimate reflection co-efficients for the mode-1 tides on realistic continental slope bathymetries, (Kelly et al. 2013a,b), but these calculations assume the incoming tide is known, and that the

slope is relatively homogenous over a long distance (presumably the mode-1 wavelength).

Determining the incident flux,  $F_{in}$ , from field data, and even from a numerical model with sufficient complexity, is not trivial. In two dimensions, or with simple plane wave geometries, it is relatively easy to fit incident and reflected plane waves and recover the desired reflection co-efficient (figure 1a). In the real ocean, even if the tidal components can be easily separated from confounding influences, internal tides are often spatially inhomogeneous, and form lateral “beams” (in x-y) that make plane wave fits difficult from a finite array of moorings; for instance the mooring array could be located more in the incoming beam than the reflected, leading to an exaggeration of the dissipation (figure 1b). Plane-wave fits to satellite altimetry tracks are promising, but will also suffer from a lack of fidelity if the internal tides are inhomogeneous on the scale of the plane wave fits. In the model, high resolution temporal and spatial information makes it possible to separate signals spectrally according to their direction of propagation (i.e. using a Hilbert transform Mercier et al. 2008), but this method works best if there are no boundaries and the signals at the edges of the model domain can be tapered to reduce leakage, neither of which are applicable here.

Here we run numerical simulations that are meant to represent a mode-1 internal  $M_2$  tide incident on the Tasman Slope, east of Tasmania. The simulations are only forced by this incident internal tide, and there is no local forcing, allowing the effect of the reflection to be teased apart. After discussing the model setup section 2, we briefly consider the response this forcing has on the slope section 3 and compute and energy budget of the complete response. In order to separate the physics of the reflection, we then simplify the geometry section 4, both geometrically, and by removing parts of the topography. This technique allows us to separate incident and reflected signals from the total response without appeal to simplified wavefits. We end with a discussion of the results (section 5) and a summary (section 6).

## 2. Model setup

### a. Basics

The numerical model used here is the MITGCM (Marshall et al. 2006). The setup is very similar to Buijsman et al. (2014), with the model run in hydrostatic mode, background (isotropic) diffusivities

and viscosities of  $10^{-5}$  m<sup>s</sup>s<sup>-1</sup>, and enhanced diffusivity and viscosity in regions of temporarily unstable stratification, as in Klymak and Legg (2010). A second-order flux-limiting temperature advection scheme is used which results in some numerical dissipation and diffusion.

Topography is from a data set that combines Smith and Sandwell (1997) and multibeam data from ??HARPER?? (figure 2b). For this paper, we use a cartesian co-ordinate system centered at 44S, 148 E, with  $y$  pointing 12 degrees east of geographic north (magenta lines figure 2). This co-ordinate system is close to cross-slope in the x-direction, and is used for conceptual convenience. The simulations are run on a f-plane ( $f = -10^{-4}$  s<sup>-1</sup>), so no planetary beta effect has been included.

Relatively high lateral resolution is used along the continental slope (figure 3a, smallest inset green box) of  $\delta x = \delta y = 1$  km. Resolution is expanded by 3.5% per grid cell beyond the high-resolution region, to a maximum of 5 km in the second largest inset box (figure 3a); this keeps the resolution over the Tasman Rise and the rest of the continental slope at least 5 km. Further out, the grid spacing is again increased at 3.5% per grid cell until a maximum grid cell size of 10 km is reached.

Vertical resolution is approximately stretched so  $dz \sim N$ , where  $N^2(z) = -\frac{g}{\rho_0} \frac{d\rho}{dz}$  is the vertical stratification. 200 vertical grid cells are used for these simulations. The vertical stratification is from the World Ocean Atlas for the Tasman Sea just offshore of Tasmania (Boyer et al. 2013), and is assumed laterally constant in the domain. This precludes any mesoscale effects, which are believed to be important in this area, and are the subject of future work.

### *b. Forcing*

To simplify the generation problem we apply an analytical forcing to our model. This is composed of two line sources at approximately the location of the Macquarie Ridge (figure 3a). The initial conditions and the southern and eastern boundaries of the model were set with this forcing. The forcing is based on (Rainville et al. 2010), except instead of a single point source placed a distance  $R$  from the line source, the line source is digitized as a number of discrete point sources and their response in the domain summed. The

mode-1 pressure anomaly is given by:

$$p'(x, y, t) = \sum_{i=1}^N a_i \exp(j(|k_t|r_i - \omega t)) \quad (1)$$

where  $r_i = \sqrt{(x - x_i)^2 + (y - y_i)^2}$  is the distance to the source, and  $|k_t|$  is the absolute value of the mode-1 wavenumber:

$$k_t = \frac{(\omega^2 - f^2)^{1/2}}{c_e} \quad (2)$$

where  $\omega$  is the frequency of the tide,  $f$  is the Coriolis frequency, and  $c_e$  is the eigenspeed of the vertical mode equation:

$$\frac{d}{dz} \left( \frac{1}{N^2} \frac{d\psi}{dz} \right) + \frac{1}{c_e^2} \psi(z) = 0. \quad (3)$$

Here  $\psi(z)$  is the eigenfunction that sets the shape of the vertical mode, and the boundary conditions are  $d\psi/dz = 0$  at  $z = 0$  and  $z = -H$ , where  $H$  is the water depth. For convenience, we normalize  $\psi_m(z)$  so that

$$\int_{-H}^0 \psi_m^2(z) dz = 1. \quad (4)$$

Horizontal velocities can be linearly decomposed by these shapes, as can the pressure signal; vertical velocities, and displacements are decomposed by the derivative of the normalized  $\psi_m$ :  $d\psi_m/dz$ .

To compute the wavefield, the horizontal velocity components are derived from the internal wave consistency relations:

$$u(x, y, t) = \sum_{i=1}^N \frac{k_x \omega + j k_y f}{\omega^2 - f^2} \frac{p'_i}{\rho} \quad (5)$$

$$v(x, y, t) = \sum_{i=1}^N \frac{k_y \omega - j k_x f}{\omega^2 - f^2} \frac{p'_i}{\rho} \quad (6)$$

where  $k_x = k_t \cos(\theta_i)$  and  $k_y = k_t \sin(\theta_i)$  are calculated from the angle to each element of the line sources  $\theta_i = \arctan((y - y_i)/(x - x_i))$ .

The resulting incoming wavefield (figure 3a) has a beam of energy flux that radiates northwest, and is relatively tightly focused. The interference pattern creates a null to the south and north, and a secondary beam that radiates due west. This schematic agrees with more realistic regional tidal models, and the amplitude of the beam was tuned to give approximately  $7 \text{ kW m}^{-1}$  of flux incident at Tasmania in the pictured realization. Most runs below were scaled to have weaker (more linear) fluxes, with approximately

$2 \text{ kW m}^{-1}$  at Tasmania, but exactly the same spatial pattern. The initial condition is applied uniformly through the domain, regardless of bathymetry, so there are some start-up transients as the proper baroclinic flow develops.

This forcing is applied on the eastern and southern boundaries of the domain. The northern and western boundaries are sponges where the velocity is slowly dropped to zero and the stratification relaxed to the initial stratification (figure 3a, green rectangles). Our main focus is the area from  $y=0$  to 400 km, so the boundaries are sufficiently far that small residual reflections do not affect the response.

The ideal response off the Tasman topography would be as a plane-wave reflection from a wall at  $x = 0 \text{ km}$  (i.e. Johnston et al. 2015). Here we have a relatively confined beam, but we can make a start by considering the reflection the beam from a wall at  $x = 0 \text{ km}$  for  $y > 0 \text{ km}$  (figure 3b,c) using the method of images with identical line sources mirrored about the  $y$ -axis, and their phase shifted by 180 deg. The reflection pattern that sets up is not entirely regular, but has some straight-forward features. The incoming beam impacts the wall at approximately 30 deg. The horizontal wavelength of an  $M_2$  internal tide is 178 km, so the standing wave in the  $x$ -direction will have a wavelength  $178/\cos(30) \approx 200\text{km}$  and in the  $y$ -direction will have a wavelength of approximately 350km. These spatial scales are readily apparent in the analytical forcing despite the non-plane-wave character of the idealized forcing (figure 3c).

### 3. Realistic model simulation

The response of the forcing in the most complex domain motivates the more idealized experiments that follow. From the initial forcing (figure 4a), a complex wavefield develops with clear scattering from the Tasman Rise, the shelf, and numerous small inhomogeneities on the sea floor (figure ??b-d). Looking along shelf, the phase of the velocity signal can be seen changing approximately every 200 km, and it changes approximately every 100 km offshelf.

This sets up a complicated interference pattern that shows inconsistent cross-slope fluxes and peaks and nulls in the along-slope fluxes to the north, as we might expect from an oblique standing wave (compare figure 4h to figure 3b). However the pattern is complicated, with offshore peaks at approximately the correct

spacing offshore, but not lining up precisely in the north-south direction. There are inhomogeneities in the energy that are not accounted for by a simple two-wave model.

An energy balance is performed on the model using the terms outlined in Kang and Fringer (2012); Kang (2011). Their energy balance vertically integrated can be schematicized as:

$$dE_{bc}/dt = -\nabla_H \mathbf{F}_{bc} + \text{Conversion} - \text{Dissipation}. \quad (7)$$

where  $E_{bc}$  is the depth-integrated baroclinic energy density,  $\mathbf{F}_{bc}$  is the depth integrated energy flux, including both the pressure work term and the non-linear advection of energy (which is small in our runs). “Conversion” is a complex term representing transfer from barotropic motions to baroclinic (Kang 2011, eq. 5.102) and includes the barotropic heaving of the water column, the density anomaly, and a non-linear horizontal advection term. The non-linear terms can be non-trivial in real bathymetry (Buijsman et al. 2014). The conversion term is positive if the barotropic tide loses energy and the baroclinic tide gains energy. “Dissipation” is computed here as the residual, and includes dissipation due to interior viscosity, numerical dissipation, bottom drag, and diffusion of energy (small).

Of note in the energy calculation is that the largest local term in the energy budget is an alternating pattern of barotropic-baroclinic conversion at the shelf break balanced by baroclinic flux convergences and divergences (figure 5). The importance of the barotropic-baroclinic term can also be seen by considering the x-integral of the energy budget from  $x = -50$  km to  $+100$  km (figure 6). Recall that the simulations have no barotropic forcing. This coupling is catalyzed by a start-up transient hitting the slope with the incoming internal tide beam, and continues throughout the simulation, and is probably a leaky super-inertial slope wave (see section 5).

The time series of the energy terms integrated along the shelf demonstrates that the barotropic-to-baroclinic term is relatively small when averaged, with a small loss of energy from the baroclinic tide to the barotropic in the integral region (figure 6b). The model is largely in a steady state by tidal cycle 15, with some residual oscillations in  $dE/dt$  and the flux convergence. The large-scale baroclinic energy changes do not change the dissipation residual very much, which is relatively constant after 5 tidal cycles. To put the 50 MW of dissipation into context, the initial energy that comes in the east and south sides of this analysis box in the initial conditions is 315 MW, so the model is dissipating about 17% of the incoming energy.

However, note that the dissipation is not the focus of these model runs nor of this paper. The forcing here is approximately a factor 3 lower than the real forcing, so its likely the fraction of dissipation at this site is higher (probably closer to 25%) if real forcing is used.

The majority of the energy budget is in the first vertical mode (figure 6c). Net fluxes in the region directly offshore of the shelf break ( $0 < x < 80$  km, and  $0 < y < 400$  km) are composed of substantial mode-1 energy converging on the shelf (95 MW net), and some reflected energy escaping in higher modes (28.3 MW, mostly in modes 2–4). The 95 MW net flux is made up of the incoming and reflected mode-1 energy, and separating those fractions out is the subject of the next section. There is some incoming higher-mode energy as well due to scattering from the Tasman Rise, but as we will also show below, this is minor. The spatial pattern (not shown) of the mode conversion at the continental slope indicates hot-spots for conversion. Modes 2 and 4 have a hotspot of conversion near  $y = 250$  km, and Mode 3 at  $y = 325$  km.

## 4. Simplified geometries

To help tease apart the effects of the Tasman Rise and the non-uniform shelf, we carry out a few simplified geometric experiments (figure 7;figure 8). The REAL case is the one discussed above (figure 8f). The NO TOPO case has no topography at all (figure 8a), just the beam being forced at the south and east boundaries and (mostly) absorbed at the west and north. RISE was run with the real bathymetry west of  $x = 70$  km (figure 8e). Three idealized geometries simplify the physics even more: the SHELF case has a supercritical two-dimensional continental shelf running north from  $y = 0$  km (figure 8d). ROUND RISE is a 1700-m tall cylinder-shaped bump with radius of 50 km centered at approximately the same location as the Tasman Rise, with no shelf to the west (figure 8b). The simplified shelf and the rise are both used in the SHELF/RISE case (figure 8c).

### a. Shelf-only configuration

The simplest topography is the SHELF configuration (figure 8d). Here we have a response that is quite similar to the analytical response calculated above (figure 3b). The only difference between these two cases

is the narrow shelf west of  $x = 0 \text{ km}$  and the slight slope to the continental slope. The interference pattern between the incoming wave and the reflected wave is clear in this plot, with the same characteristic length scales as above, and a slight bending of the response due to the radial spreading of the beam.

The goal of this paper is to determine the amount of reflectivity of the continental slope. This is a hard number to determine in a complicated geometry, and naturally depends on the region of integration. For the SHELF configuration the situation is relatively simple, and we use it to illustrate the numerical technique used below. The signal in the full simulation is assumed to consist of an “incoming” signal and a reflected signal, so we can decompose the east-west velocity amplitude of the first vertical mode (for example) as:

$$u_1^t(x, y) = u_1^i + u_1^r \quad (8)$$

$$v_1^t(x, y) = v_1^i + v_1^r \quad (9)$$

$$p_1^t(x, y) = p_1^i + p_1^r \quad (10)$$

where  $u_1^t$  is the complex amplitude of the  $M_2$ , mode-1 east-west velocity of the simulation with the reflection,  $u_1^i$  of the incoming signal, and  $u_1^r$  of the reflected signal. We assume for this example that the incoming signal  $u_1^i$  is given by the NO TOPO simulation, and  $u_1^t$  is from the SHELF simulation. The reflected signal  $u_1^r$  is simply the difference of these two.

In order to compute and energy budget, we consider that the energy fluxes are calculated from the decomposed signals as:

$$P_{u1}^t = u_1^t p_1^t \quad (11)$$

$$= \underbrace{u_1^i p_1^i}_{\text{Incoming}} + \underbrace{u_1^r p_1^r}_{\text{Reflected}} + \underbrace{u_1^i p_1^r + u_1^r p_1^i}_{\text{Cross Terms}} \quad (12)$$

$$P_{v1}^t = v_1^t p_1^t \quad (13)$$

$$= \underbrace{v_1^i p_1^i}_{\text{Incoming}} + \underbrace{v_1^r p_1^r}_{\text{Reflected}} + \underbrace{v_1^i p_1^r + v_1^r p_1^i}_{\text{Cross Terms}} \quad (14)$$

The cross terms are not negligible for any realistic forcing, and indeed give rise to the interference patterns seen above, and is a consequence of rotation’s influence on the internal waves (Nash et al. 2004; Martini et al. 2007).

The “total” response (figure 9d) consists of the incoming response (figure 9a), and the “reflected” signal

(figure 9b), and substantial cross-terms (figure 9c). The cross terms are mostly perpendicular to the direction of reflection (i.e. perpendicular to the shelf) and alternate fluxing energy to the north and south every half cross-shelf wavelength. Combined, these three components give the “total” flux with net fluxes to the north in alternating peaks every full offslope wavelength.

The reflected response (figure 9b) shows approximately what we would expect with energy being radiated to the north-east. There is some concentration of this energy at  $y \approx 75\text{km}$ , and  $y \approx 225\text{km}$ . As above, this is because of coupling with a slope wave that is strummed by the initial conditions. This coupling causes a redistribution of the reflected energy, focusing it approximately every along-slope wavelength of the shelf wave (we show below that this wavelength changes as the shelf geometry changes).

Performing this analysis for the lowest 10 modes, we arrive at an energy budget for the shelf in the green box in the figures ( $0 < y < 400\text{ km}$ , and  $x < 80\text{ km}$ ; figure 9, inset budgets). Note that we assume the flux through  $x = 0$  is zero. With this calculation, we see that 408 MW is incident on the shelf in mode-1. There is also a net flux of 50 MW into this region from the cross terms. This is a redistribution of energy from north of our box into the box. There is a net convergence of this cross-term energy because there is dissipation in the box; in a purely inviscid solution this term should balance to zero over a closed box. If we move the integration further north, the cross-term flux drops to zero.

Most of the incoming energy reflects back out of the box (figure 9b), with the bulk remaining in mode 1, and some scattering to higher modes due to the shelf. This scattered energy reflects to the north east (not shown). The mode-1 reflection is affected by a shelf wave that transfers energy to and from the barotropic tide along the slope, resulting in nulls and peaks in the mode-1 reflection.

#### *b. Tasman Rise only*

The Tasman Rise has a profound effect on the energy that impacts the continental slope, as well as having some back reflection (figure 8e and f). The incoming beam is almost 500 km wide at  $x = 0$  if there is no Tasman Rise, but breaks into three narrower beams when there is a Tasman Rise (figure 8e). Upstream of the rise, the effect is somewhat less energy propagating westward, with an interference pattern towards the east indicating some back reflection.

This pattern can be explained in terms of diffraction of the internal tide beam from a deep obstacle (i.e. Johnston and Merrifield 2003). There is a down-wave concentration of energy along the seamount's axis, a null, and sidelobes to the north and south. In this case, the incident beam is of comparable size to the obstacle, leading to an asymmetry, and a stronger lobe to the north than south.

Most of the response due to the Tasman Rise can be modeled simply as a cylindrical obstacle in the beam (figure 8b and c). Here our obstacle is 1800 m high in 5000 m of water, and has a radius of 50 km (figure 7). This captures most of the features of the actual Tasman Rise, despite not having a shallow spire in the center and being slightly smaller than the real Rise. The differences make the simplified response have weaker nulls and the whole response is directed a bit further north than the real Rise. Adding the shelf (figure 8c) yields a response that bears substantial similarity to the REAL forcing case.

Decomposing into an incoming and reflected signal (figure 10) demonstrates the effect of the Tasman Rise on the response. Less energy is incident on the control volume, largely because the diffraction redirects some of that energy to the north of  $y = 400\text{km}$ . There is a strong reflection of energy where the main diffraction lobe reflects from the slope (figure 10b), and a smaller maximum just to the north ( $y = 250\text{km}$ ) due to the along-shelf wave that is strummed. There is a reflection further north where the northern lobe of the diffraction pattern reflects.

The incoming energy has some more higher mode content due to scattering at the cylindrical rise (figure 10a), though it is still 95% mode-1. The reflection is almost 80% mode-1, with some scattering to higher modes. The net flux shows approximately 15% of the incoming energy is dissipated at the shelf.

### *c. Real Case*

The REAL forcing is similar, if more complex (figure 11). The simulation using the bathymetry in the RISE ONLY case (figure 8e) is used as the "Incoming" energy flux, and the REAL (figure 8f) case is the "Total". Compared to the cylindrical rise, the real Tasman Rise creates a sharper diffraction pattern, and more back reflection. However, the REAL simulation has many of the same features as the RISE AND SHELF simulation (figure 8c).

Slightly less incoming energy passes into the control volume (figure 11a) because the diffraction by the

real Tasman Rise is sharper than the cylindrical rise. As for the cylindrical rise case, there is some incoming higher mode energy due to forward scattering, though again over 95% is mode-1. Reflection is concentrated near  $y = 125$  km and  $y = 450$  km, associated with the diffraction nodes, with about 85% in mode 1 (figure 11b). Dissipation is less than 25% of the incoming energy (figure 11d).

## 5. Discussion

### a. Scattering from linear calculations

The fraction of reflected tide can be predicted from linear theory to relatively good approximation using the method described by Kelly et al. (2013b) of matching Laplacian tidal solutions at discrete steps on a discretized topography. Their work originally only considered tides normally incident to the topography, but oblique incidence is straight forward to calculate using the same numerical method, taking into account that the wavenumber normal to the topography is given by  $k = K \cos \theta$ . Oblique incidence makes a substantial difference in the modal distribution of the reflected tide, with more oblique reflections scattering less energy to higher modes for the topography used in the SHELF case (figure 12). At normal incidence for this shelf shape and stratification 75% of the incoming energy reflects as mode 1, whereas for  $30^\circ$  incidence, it is closed to 85%, and reaches almost 100% as incidence increases. Agreement between the full numerical simulation and the linear model is good, though there is less energy in mode 2 and more in mode 3 in the model than the linear prediction. Interestingly, most of this increased mode-1 reflection is at the expense of mode-2.

Linear reflection from the real topography is quite variable, depending on the two-dimensional topography chosen and the angle of incidence (figure ??). Note that as the angle of incidence increases the standing wave's horizontal wavelength in the  $x$  direction increases. However also note that high mode reflected response has the same  $x$  direction wavelength. The response at  $y = 240$  km goes through a significant scattering into higher modes and dissipation, with only 28% of incoming mode-1 energy reflecting as mode-1. Interestingly this number drops dramatically as the incident angle increases from 30 to 60 degrees.

The variability of reflectivity along the slope is considerable (figure 14), with values ranging from 9% to 96%. However, much of the slope where the diffracted energy is the strongest ( $y \approx 125$  km and  $y \approx 425$  km) is

also where the incoming energy in the means is the strongest, so when weighted by the forcing we expect the overall reflectivity to be approximately 80%. In the REAL numerical run, the reflectivity into mode-1 is only about 67%, so somewhat less. The differences are likely due to dissipation and possibly three dimensionality of the reflection pattern.

*b. Slope wave importance and dynamics*

The structure of the barotropic-to-baroclinic conversion on the slope is an intriguing feature of these simulations. It shows up most clearly in the SHELF simulations because of the simplified bathymetry. However, it is also clear in the REAL simulation (figure 5a). This slope wave redistributes energy in the reflected baroclinic response (figure 9), taking a relatively homogenous incoming energy source and focusing the reflection every 200 km or so along shelf.

This wave is a slope mode that is strummed by the incident internal tide at the “corner” of the topography ( $x = 0, y = 0$ ); a long shelf without the corner does not excite this wave, nor does an internal tide coming directly from the east and hitting the topography at a normal angle. The along-slope wavelength is independent of the along-slope wavelength in the open water (tested by changing the angle of the incident tide), and is a robust feature of the shelf shape. Wider shelves have shorter along-slope wavelengths, and narrow shelves have longer (figure 15).

These waves are superinertial, and hence not traditional subinertial coastally trapped waves (i.e. Brink 1991). However, Dale and Sherwin (1996) show that superinertial waves on continental slopes can still have modes that grow more rapidly in frequency and along-slope wavenumber. Here our frequency is fixed, so we expect there to be resonant along-slope wavenumbers. The vertical-cross slope response of these waves, or modes, are basically a local mode-1 in the deep ocean, and close to barotropic on the shallow shelf, matching our findings here.

These slope modes transfer energy from the mode-1 internal tide to the barotropic (in our local accounting). Because the waves are super-inertial, they are not perfectly trapped on the slope, and require forcing to keep their energy, and re-radiate energy offshore. Calculating how much energy is redistributed as a function of the shelf-wave amplitude is an interesting problem that will require further research.

## 6. Summary

A mode-1 internal tide was launched at a variety of topographies representing the Tasmanian continental slope. The goal was to determine the “reflectivity” of this slope, in terms of the modal content of the reflected energy and the local dissipation. The latter is somewhat suspect in this model because of crude lateral resolution, but the REAL simulation indicated that 21% of the incoming energy was dissipated, and 65% was reflected as mode-1 energy. The incoming internal tide flux used here was weak compared to the flux modeled and inferred from altimetry in the Tasman Sea, so we expect the dissipation in more strongly forced models to increase.

Despite a relatively simple incoming internal tide which is linear, semi-diurnal, and mode-1, we have found a rich and complex response of the topography when the remote wave impacts the topography east of Tasmania. The response can be characterized as follows:

- Diffraction of the beam by the Tasman Rise,
- oblique reflection from the continental slope,
- and a forced slope wave response that redistributes reflected internal energy along-slope.

Of these, perhaps only the second effect was expected before carrying out the simulations. However, as we saw above, even the reflection problem is significantly complicated in the presence of three-dimensionality, such that it is difficult to determine the appropriate slope for the incoming wave to impact the shelf.

Diffraction around underwater topography should have been expected, however, the relative depth of the obstacle makes it surprising that the effect is so strong. The fact that the size of the Tasman Rise is close to that of a wavelength of the incoming internal tide makes predicting the diffraction pattern difficult. Baines (2007) considers generation of internal tides at seamounts, but does not deal with scattering and diffraction. The problem is similar to electromagnetic waves passing through a wire, but a linear response for that problem is not trivial to compute (i.e. Bonod et al. 2005), and still does not have a confined vertical mode structure as we find in the internal wave problem.

The excitation of slope waves is a nice corroboration of theory by Dale et al. (2001), and it has a low-order effect on the redistribution of energy along slope. If the dissipation in this crude model is to be believed (and

we feel it is actually close, based on higher resolution runs), the redistribution affects where high dissipation is found (figure 5). Finally, it adds more inhomogeneity to the reflected internal tide.

The complexity grows if other real-world influences are to be accounted for. The East Australian Current flows along this slope, varying the stratification in the horizontal, provides lateral shears that can distort the internal tide response, and carrying eddies that can add a strong time dependence to these effects. Even in two dimensions, the strength of the internal tide reflection can be significantly impacted by the phase of the incoming tide with other baroclinic modes Klymak et al. (2011) or the barotropic (Kelly and Nash 2010). The simulations here exclude the local barotropic tide, so this would certainly complicate the reflected response. Finally, the internal tide used here was monotonic, whereas the real tide will have other frequencies, most notably subinertial diurnal frequencies that will have trapped wave responses (personal communication, R. Musgrave).

Regardless, it is useful to have separated the “simplest” response we could in this system to tease apart the dominant physics. This response is complex enough as it is that it should be clear that solely observational efforts to balance a reflection budget are going to be a challenge. Merging simulations and observations is a likely way forward in understanding the wave field in this complex slope region.

#### *Acknowledgments.*

Start acknowledgments here.

## REFERENCES

- Baines, P. G., 2007: Internal tide generation by seamounts. *Deep Sea Res. I*, **54** (9), 1486 – 1508, doi: <http://dx.doi.org/10.1016/j.dsr.2007.05.009>, URL <http://www.sciencedirect.com/science/article/pii/S0967063707001306>.
- Bonod, N., E. Popov, and M. Nevière, 2005: Differential theory of diffraction by finite cylindrical objects. *JOSA A*, **22** (3), 481–490.
- Boyer, T., et al., 2013: *World Ocean Database 2013*. NOAA Atlas NESDIS 72, doi:10.7289/V5NZ85MT.
- Brink, K., 1991: Coastal-trapped waves and wind-driven currents over the continental shelf. *Annu. Rev. Fluid Mech.*, **23**, 389–412.
- Buijsman, M. C., et al., 2014: Three-dimensional double-ridge internal tide resonance in Luzon Strait. *J. Phys. Oceanogr.*, **44** (3), 850–869.
- Carter, G., et al., 2008: Energetics of M 2 Barotropic-to-Baroclinic Tidal Conversion at the Hawaiian Islands. *Journal of Physical Oceanography*, **38** (10), 2205–2223.
- Dale, A. C., J. M. Huthnance, and T. J. Sherwin, 2001: Coastal-trapped waves and tides at near-inertial frequencies. *J. Phys. Oceanogr.*, **31** (10), 2958–2970.
- Dale, A. C. and T. J. Sherwin, 1996: The extension of baroclinic coastal-trapped wave theory to superinertial frequencies. *J. Phys. Oceanogr.*, **26** (11), 2305–2315.
- Johnston, T. M. S., D. L. Rudnick, and S. M. Kelly, 2015: Standing internal tides in the Tasman Sea observed by gliders, doi:<http://www-pord.ucsd.edu/~shaunj/files/standing20150528.pdf>, in press *J. Phys. Oceanogr.*
- Johnston, T. S. and M. A. Merrifield, 2003: Internal tide scattering at seamounts, ridges, and islands. *J. Geophys. Res.*, **108** (C6), 3180, doi:10.1029/2002JC01528.

- Kang, D., 2011: Barotropic and baroclinic tidal energy. Ph.D. thesis, Stanford University.
- Kang, D. and O. Fringer, 2012: Energetics of barotropic and baroclinic tides in the monterey bay area. *J. Phys. Oceanogr.*, **42** (2), 272–290.
- Kelly, S. and J. Nash, 2010: Internal-tide generation and destruction by shoaling internal tides. *Geophysical Research Letters*, **37**, L23 611.
- Kelly, S. M., N. L. Jones, and J. D. Nash, 2013a: A coupled model for laplace's tidal equations in a fluid with one horizontal dimension and variable depth. *Journal of Physical Oceanography*, **(2013)**.
- Kelly, S. M., N. L. Jones, and J. D. Nash, 2013b: A coupled model for laplace's tidal equations in a fluid with one horizontal dimension and variable depth. *Journal of Physical Oceanography*, **(2013)**, doi: 10.1175/JPO-D-12-0147.1.
- Klymak, J., M. Alford, R. Pinkel, R. Lien, Y. Yang, and T. Tang, 2011: The breaking and scattering of the internal tide on a continental slope. *J. Phys. Oceanogr.*, **41**, 926–945, doi:10.1175/2010JPO4500.1.
- Klymak, J. M. and S. M. Legg, 2010: A simple mixing scheme for models that resolve breaking internal waves. *Ocean Modell.*, **33** (3-4), 224 – 234, doi:10.1016/j.ocemod.2010.02.005.
- Klymak, J. M., et al., 2006: An estimate of tidal energy lost to turbulence at the Hawaiian Ridge. *J. Phys. Oceanogr.*, **36**, 1148–1164.
- Legg, S. and J. M. Klymak, 2008: Internal hydraulic jumps and overturning generated by tidal flow over a tall steep ridge. *J. Phys. Oceanogr.*, **38** (9), 1949–1964.
- Marshall, J., E. Shuckburgh, H. Jones, and C. Hill, 2006: Estimates and implications of surface eddy diffusivity in the Southern Ocean derived from tracer transport. *J. Phys. Oceanogr.*, **36** (9), 1806–1821.
- Martini, K., M. Alford, J. Nash, E. Kunze, and M. Merrifield, 2007: Diagnosing a partly standing internal wave in Mamala Bay, Oahu. *Geophys. Res. Lett.*, **34** (17), L17 604.
- Martini, K. I., M. H. Alford, E. Kunze, S. M. Kelly, and J. D. Nash, 2013: Internal bores and breaking internal tides on the oregon continental slope. *J. Phys. Oceanogr.*, **43**, 120–139.

Melet, A., R. Hallberg, S. Legg, and K. Polzin, 2013: Sensitivity of the ocean state to the vertical distribution of internal-tide-driven mixing. *J. Phys. Oceanogr.*, **43** (3), 602–615.

Mercier, M. J., N. B. Garnier, and T. Dauxois, 2008: Reflection and diffraction of internal waves analyzed with the Hilbert transform. *Phys. Fluids*, **20** (8), 086 601.

Nash, J., M. Alford, E. Kunze, K. Martini, and S. Kelley, 2007: Hotspots of deep ocean mixing on the Oregon continental slope. *Geophys. Res. Lett.*, **34**, L01 605, doi:10.1029/2006GL028 170.

Nash, J. D., E. Kunze, J. M. Toole, and R. W. Schmitt, 2004: Internal tide reflection and turbulent mixing on the Continental Slope. *J. Phys. Oceanogr.*, 1117–1134.

Polzin, K. L., 2009: An abyssal recipe. *Ocean Modelling*, **30** (4), 298–309, doi:doi:10.1016/j.ocemod.2009.07.007.

Rainville, L., T. Johnston, G. S. Carter, M. A. Merrifield, R. Pinkel, P. F. Worcester, and B. D. Dushaw, 2010: Interference pattern and propagation of the m2 internal tide south of the hawaiian ridge. *J. Phys. Oceanogr.*, **40** (2).

Smith, W. and D. Sandwell, 1997: Global sea floor topography from satellite altimetry and ship depth soundings. *Science*, **277** (5334), 1956.

St. Laurent, L. and C. Garrett, 2002: The role of internal tides in mixing the deep ocean. *J. Phys. Oceanogr.*, **32**, 2882–2899.

## List of Figures

- 1 Schematic of the difficulty of quantifying reflecting fluxes in an inhomogeneous environment.  
Plane waves are trivial. Inhomogeneous incoming waves or reflections are significantly more difficult. 22
- 2 Location of TTide experiment: a) Energy flux in a regional numerical simulation. Color is the absolute value of the flux, arrows its direction. The magenta box indicates the numerical modeling domain used in this paper. b) Detail of the bathymetry on the Tasman slope. The magenta lines indicate 100 km in the x-direction, and 300 km in the y direction in the modeling domain used in this paper. 23
- 3 a) Forcing used to drive the models used in this paper. Two mode-1 internal wave sources are located to the south east (blue lines). The model domain is rotated 12 degrees from geographic so the shelf break approximately lies along  $x = 0$ . Typical model domain and sponge region is indicated as green rectangles. The 250, and 3000-m isobaths are contoured. Arrows show the direction of the energy flux, and are scaled by its strength. b) Energy flux of analytical response of energy reflecting from a wall at  $x = 0$ , north of  $y = 0$ . c) Phase of reflected response. 24
- 4 a)–d) Surface x-direction velocity for four snapshots. a) is the initial conditions (slightly modified after a tidal cycle) and d) is the steady state. Grey contours are depths at 3000, 2000, 1000, and 250-m. e)–h) is depth-integrated baroclinic energy flux at the same time periods, with arrows indicating direction. 25
- 5 Energy budget over the 19th tidal cycle of a) Barotropic to baroclinic conversion; b) Baroclinic energy flux convergence ( $-\nabla F_{bc}$ ); c) rate of change of baroclinic energy; d) residual representing the dissipation in the model  $D = -\nabla F_{bc} + \text{Conv.} - dE/dt$ . The green box is the region for the energy time series (figure ??) 26

6 a) Integral in  $x$  to 80 km offshore of the energy terms in figure 5 for the REAL case. Note  
that the barotropic-baroclinic term (red) is of the same order as the baroclinic convergence  
(cyan) and the residual dissipation (gray) for most of the shelf. b) Energy budget time series  
for the “Real” case, tidally averaged, where time is normalized by  $T = 12.4h$ , between  $y = 0$   
to  $y = 400$  km. There is still a small residual increase in the energy with time (purple),  
representing the accumulation of high-mode energy in the region. Net barotropic-baroclinic  
conversion (red) is small and negative, indicating a small net loss to the barotropic tide in  
this region. The bulk of the budget is the balance between baroclinic flux convergence (blue)  
and the residual “dissipation” (gray). c) Net flux in the box defined by  $0 < x < 80$  km, and  
 $0 < y < 400$  km. Green is the value for the net flux (no modal decomposition). Blue bars are  
the modal decomposition. There is a net incoming flux in mode 1 and net reflecting fluxes in  
higher modes (primarily modes 2-4). 27

7 Cross sections of topographies from  $y = 50$  km. 28

8 Energy flux for six geometries at tidal cycle 20. Grey depth contours are -3000, -2000, -1000  
and -250 m. Arrows indicate the direction of energy flux. See figure 7 for bathymetry cross  
sections at  $y = 50$  km. 29

9 Mode-1 decomposition of energy fluxes for the SHELF experiment. 30

10 Mode-1 decomposition of energy fluxes for the RISE-SHELF experiment. 31

11 Energy decomposition based on taking the NO TOPO case as the incoming wave, and RISE  
as the total wavefield and looking at the energy flux of the difference between their waves  
(reflected wave field) and the energy flux associated with the cross terms between. 32

12 The reflected flux for the SHELF bathymetry (diamonds), and the results of a linear internal  
tide solution through a series of incident mode-1 angles. 33

13 Velocity snapshots from linear calculation of reflecting mode-1 internal tide from three sections  
of bathymetry, and three incident angles. 34

- 14 Strength of the reflection calculated from the two-dimensional linear method assuming an  
incident angle of 30 degrees, divided into vertical modes. Dashed lines are means of mode-  
1 reflection, centered where the main and northern lobes of the diffraction pattern hit the  
bathymetry, and one from  $y = 0$  km to  $y = 400$  km. Compare the reflectivity here with the  
67% reflectivity of mode 1 in the REAL simulation (figure 11). 35
- 15 Barotropic to baroclinic conversion for different shelf widths from widest (a) to narrowest (d).  
Arrows are barotropic flux vectors. Note how the along-slope barotropic flux is almost entirely  
confined to conversion dipoles along slope. 36

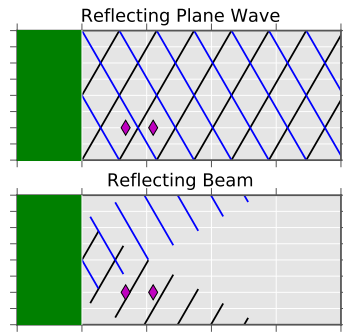


FIG. 1. Schematic of the difficulty of quantifying reflecting fluxes in an inhomogeneous environment. Plane waves are trivial. Inhomogeneous incoming waves or reflections are significantly more difficult.

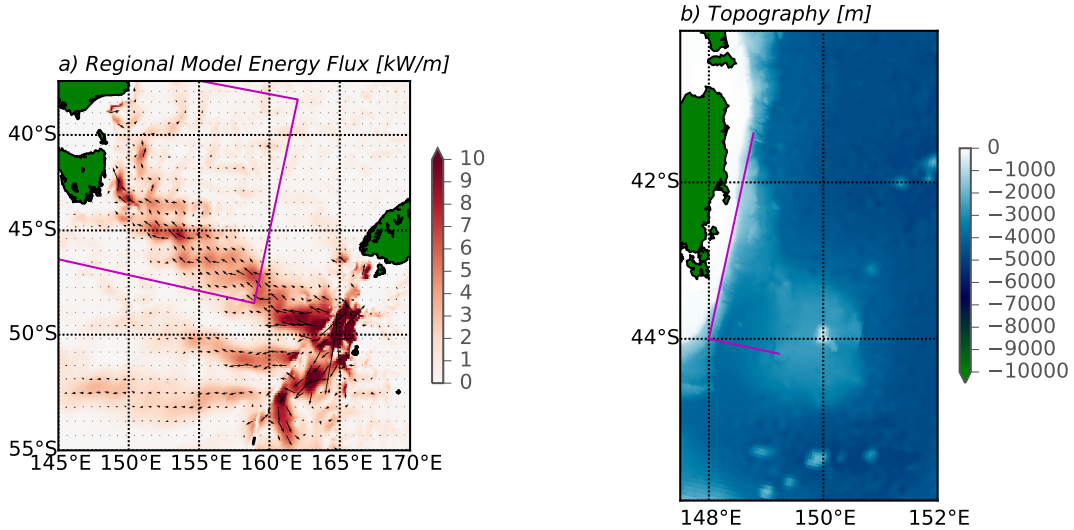


FIG. 2. Location of TTide experiment: a) Energy flux in a regional numerical simulation. Color is the absolute value of the flux, arrows its direction. The magenta box indicates the numerical modeling domain used in this paper. b) Detail of the bathymetry on the Tasman slope. The magenta lines indicate 100 km in the x-direction, and 300 km in the y direction in the modeling domain used in this paper.

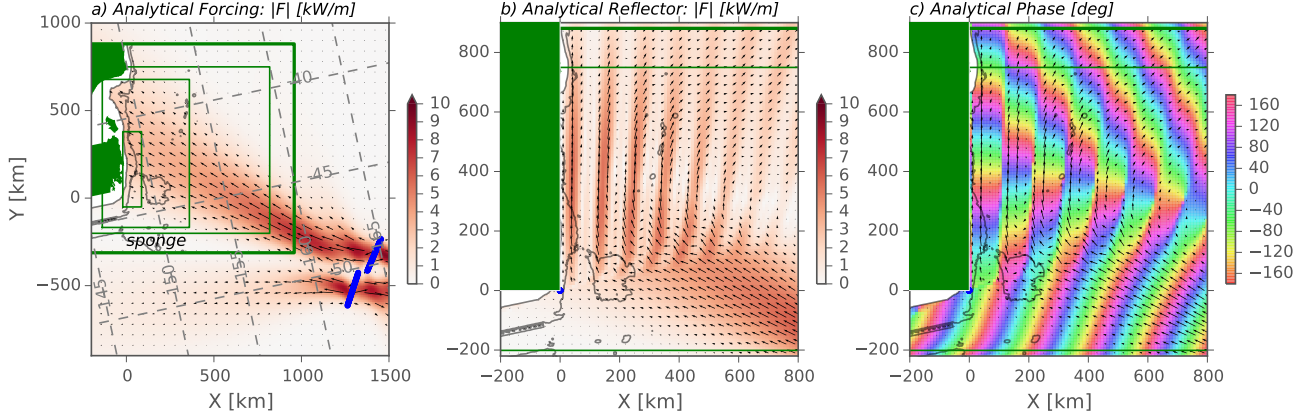


FIG. 3. a) Forcing used to drive the models used in this paper. Two mode-1 internal wave sources are located to the south east (blue lines). The model domain is rotated 12 degrees from geographic so the shelf break approximately lies along  $x = 0$ . Typical model domain and sponge region is indicated as green rectangles. The 250, and 3000-m isobaths are contoured. Arrows show the direction of the energy flux, and are scaled by its strength. b) Energy flux of analytical response of energy reflecting from a wall at  $x = 0$ , north of  $y = 0$ . c) Phase of reflected response.

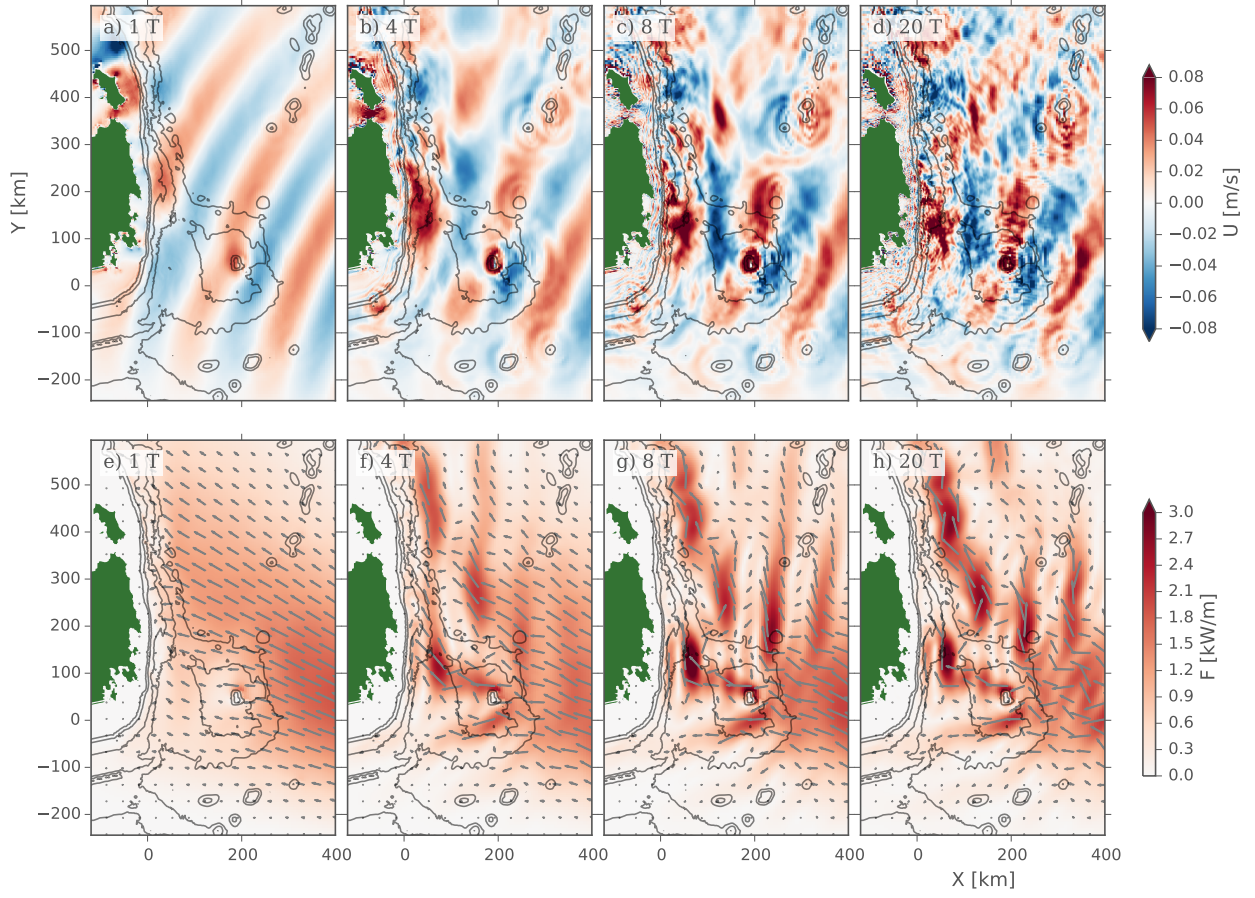


FIG. 4. a)-d) Surface x-direction velocity for four snapshots. a) is the initial conditions (slightly modified after a tidal cycle) and d) is the steady state. Grey contours are depths at 3000, 2000, 1000, and 250-m. e)-h) is depth-integrated baroclinic energy flux at the same time periods, with arrows indicating direction.

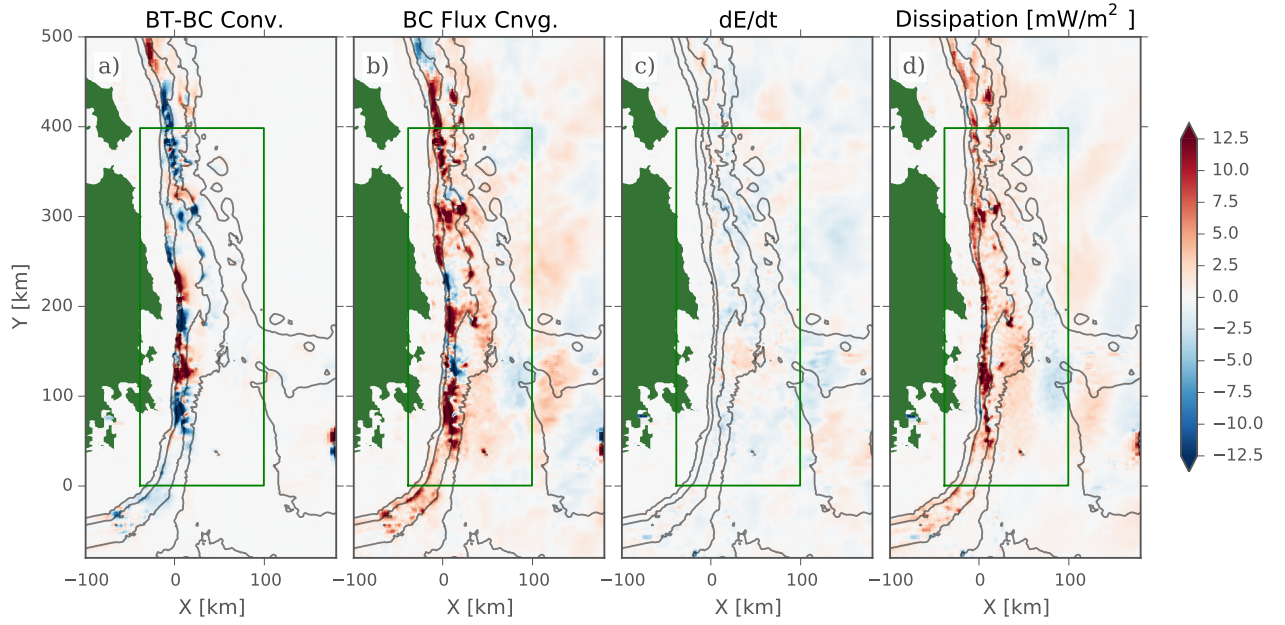


FIG. 5. Energy budget over the 19th tidal cycle of a) Barotropic to baroclinic conversion; b) Baroclinic energy flux convergence ( $-\nabla F_{bc}$ ); c) rate of change of baroclinic energy; d) residual representing the dissipation in the model  $D = -\nabla F_{bc} + \text{Conv.} - dE/dt$ . The green box is the region for the energy time series (FIG. ??)

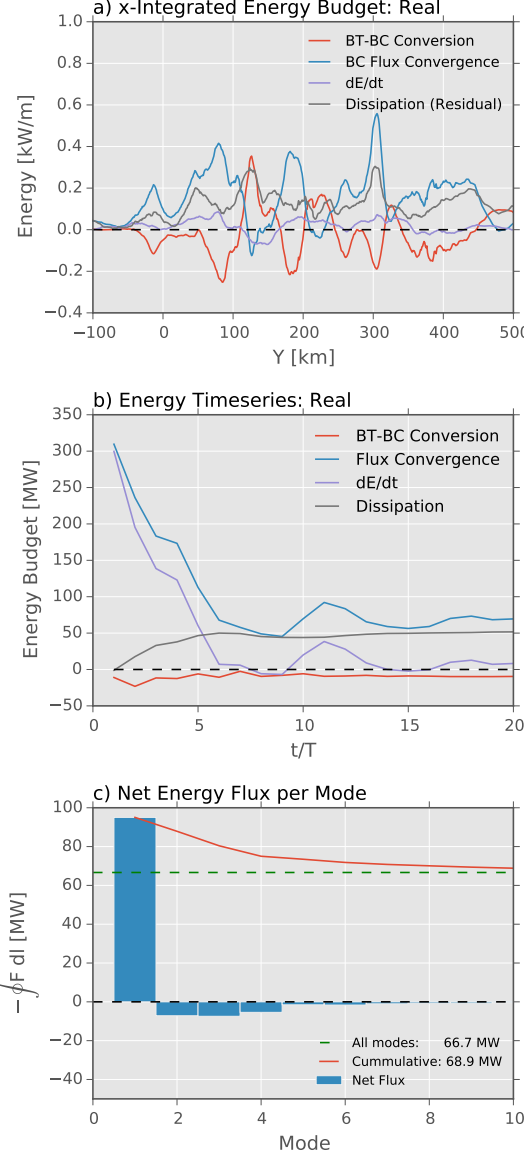


FIG. 6. a) Integral in  $x$  to 80 km offshore of the energy terms in FIG. 5 for the REAL case. Note that the barotropic-baroclinic term (red) is of the same order as the baroclinic convergence (cyan) and the residual dissipation (gray) for most of the shelf. b) Energy budget time series for the “Real” case, tidally averaged, where time is normalized by  $T = 12.4h$ , between  $y = 0$  to  $y = 400$  km. There is still a small residual increase in the energy with time (purple), representing the accumulation of high-mode energy in the region. Net barotropic-baroclinic conversion (red) is small and negative, indicating a small net loss to the barotropic tide in this region. The bulk of the budget is the balance between baroclinic flux convergence (blue) and the residual “dissipation” (gray). c) Net flux in the box defined by  $0 < x < 80$  km, and  $0 < y < 400$  km. Green is the value for the net flux (no modal decomposition). Blue bars are the modal decomposition. There is a net incoming flux in mode 1 and net reflecting fluxes in higher modes (primarily modes 2-4).

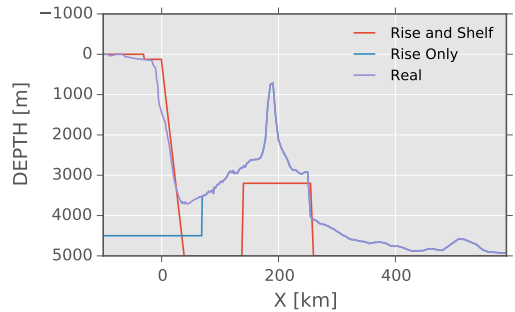


FIG. 7. Cross sections of topographies from  $y = 50$  km.

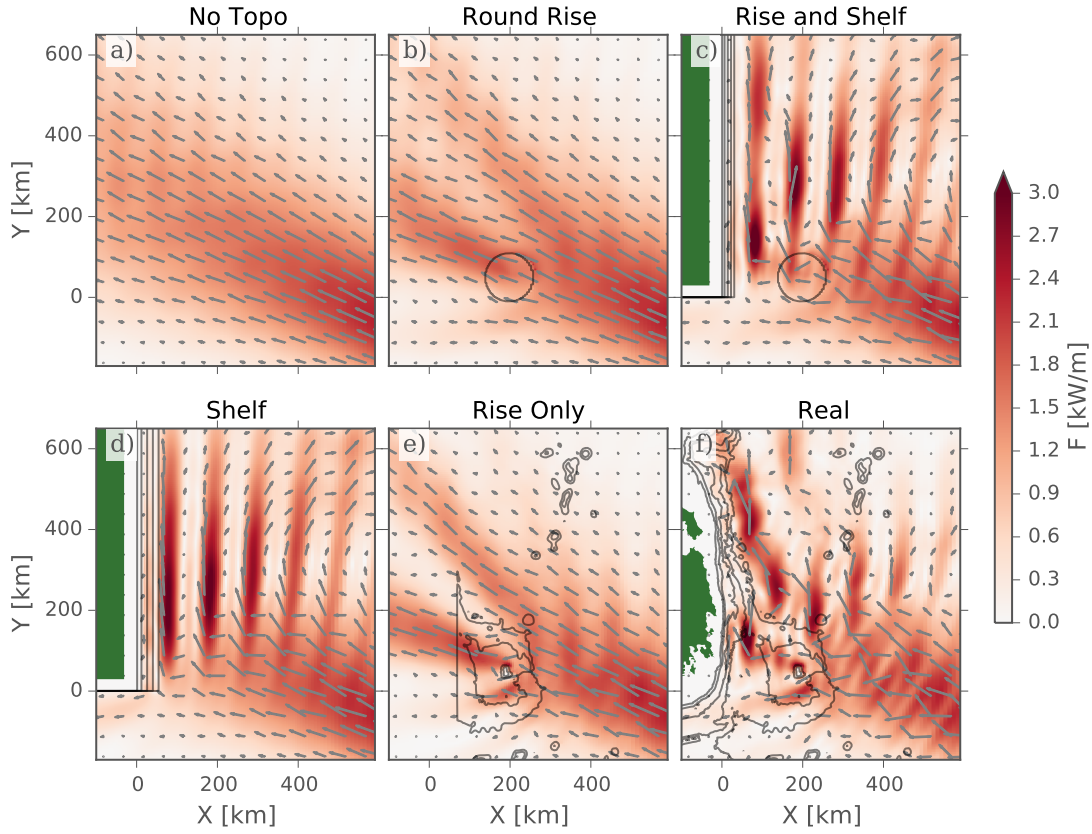


FIG. 8. Energy flux for six geometries at tidal cycle 20. Grey depth contours are -3000, -2000, -1000 and -250 m. Arrows indicate the direction of energy flux. See FIG. 7 for bathymetry cross sections at  $y = 50$  km.

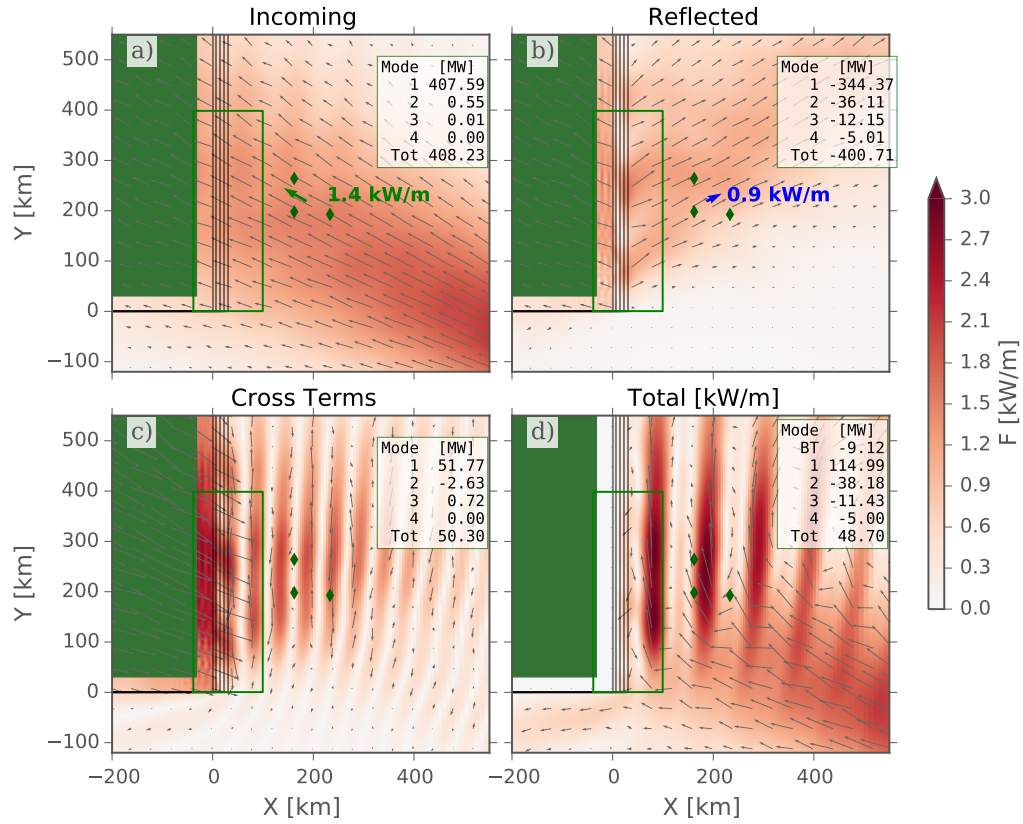


FIG. 9. Mode-1 decomposition of energy fluxes for the SHELF experiment.

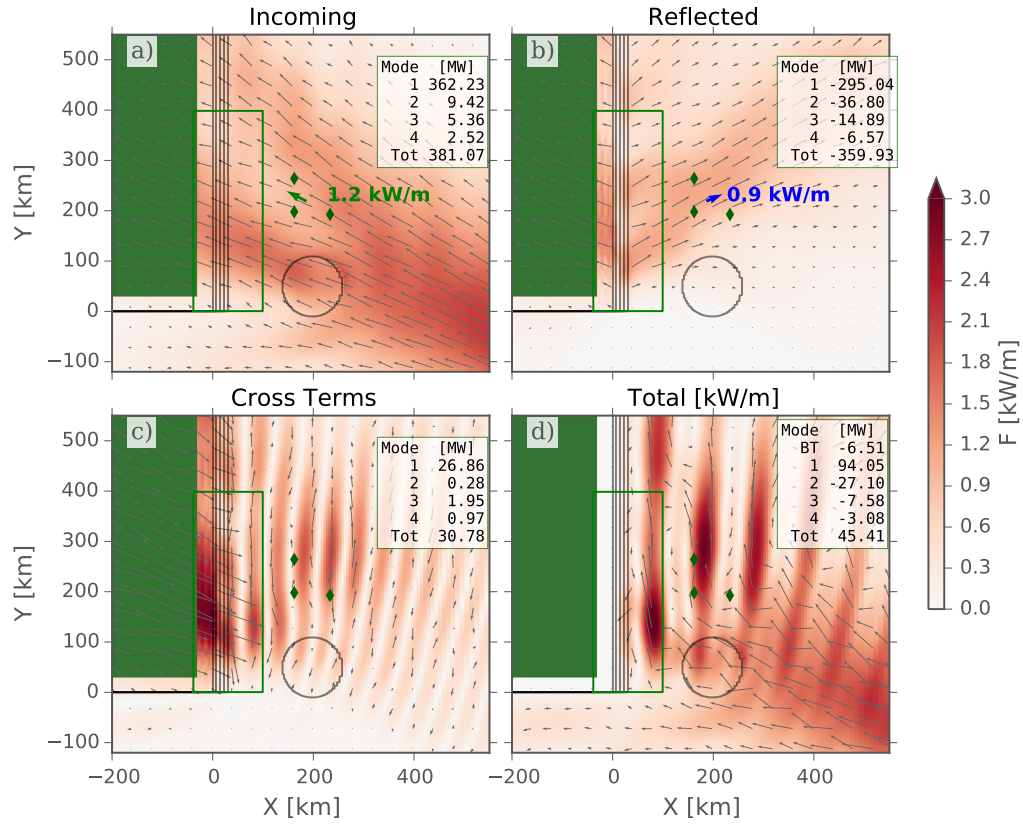


FIG. 10. Mode-1 decomposition of energy fluxes for the RISE-SHELF experiment.

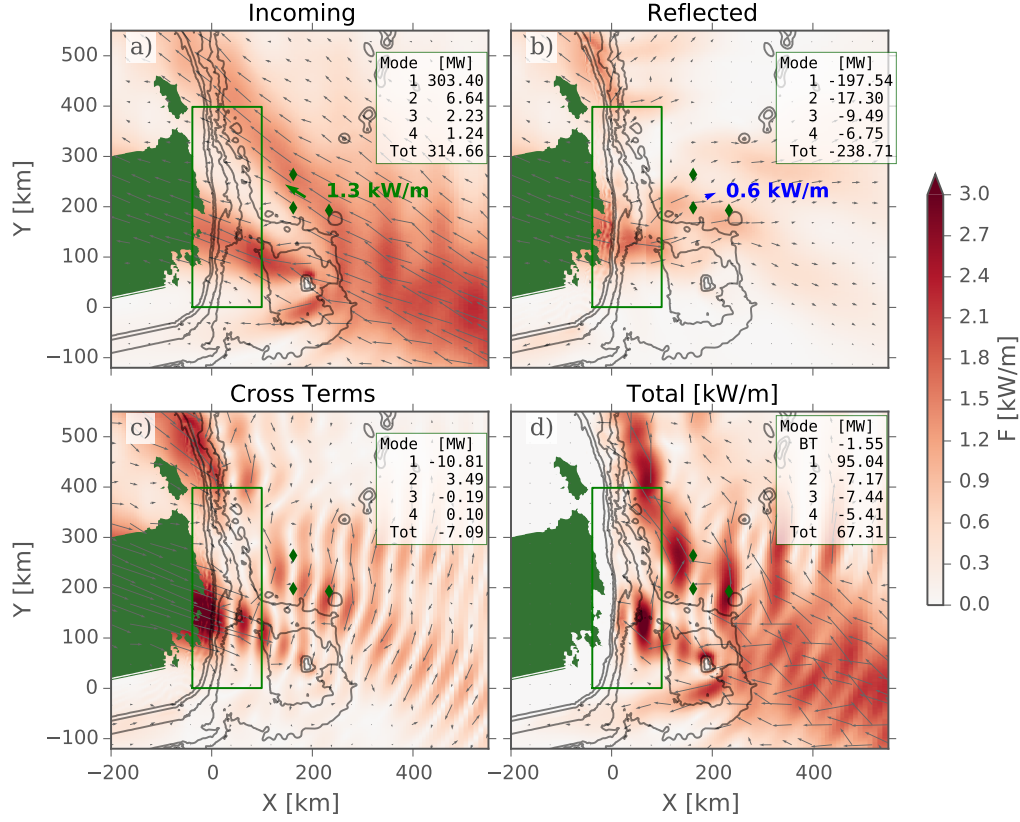


FIG. 11. Energy decomposition based on taking the No TOPO case as the incoming wave, and RISE as the total wavefield and looking at the energy flux of the difference between their waves (reflected wave field) and the energy flux associated with the cross terms between.

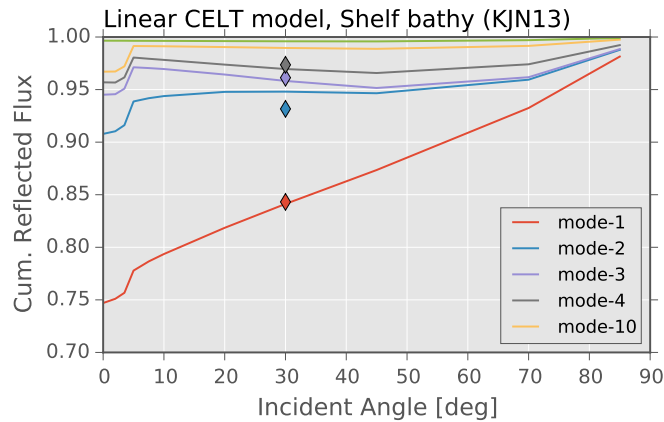


FIG. 12. The reflected flux for the SHELF bathymetry (diamonds), and the results of a linear internal tide solution through a series of incident mode-1 angles.

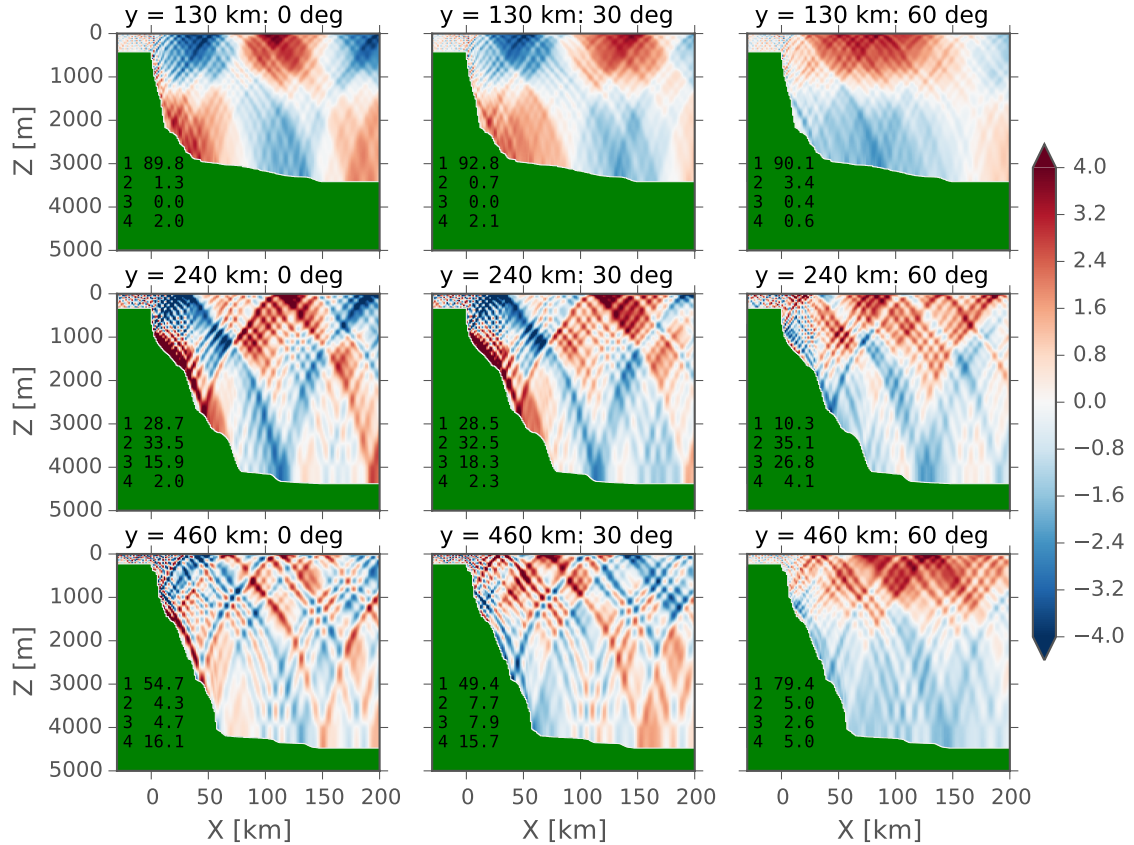


FIG. 13. Velocity snapshots from linear calculation of reflecting mode-1 internal tide from three sections of bathymetry, and three incident angles.

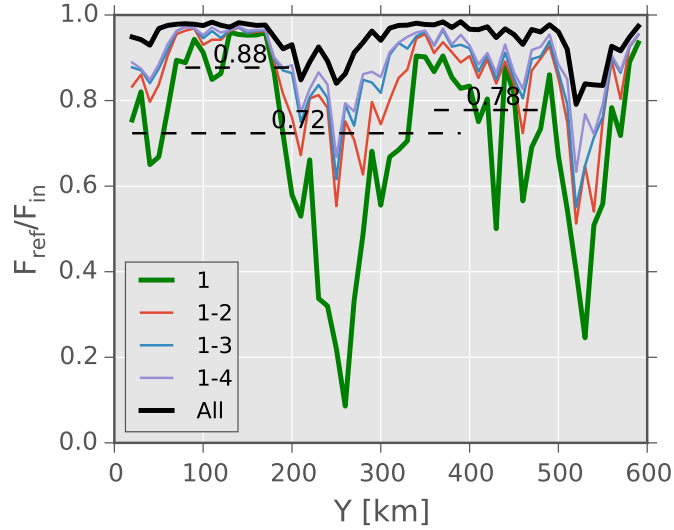


FIG. 14. Strength of the reflection calculated from the two-dimensional linear method assuming an incident angle of 30 degrees, divided into vertical modes. Dashed lines are means of mode-1 reflection, centered where the main and northern lobes of the diffraction pattern hit the bathymetry, and one from  $y = 0 \text{ km}$  to  $y = 400 \text{ km}$ . Compare the reflectivity here with the 67% reflectivity of mode 1 in the REAL simulation (FIG. 11).

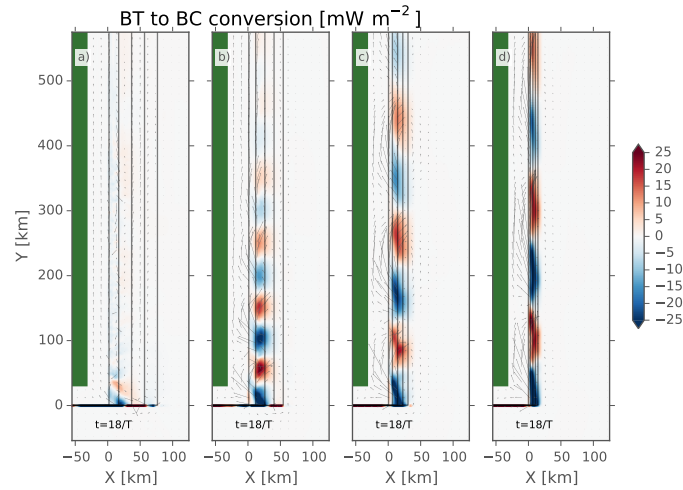


FIG. 15. Barotropic to baroclinic conversion for different shelf widths from widest (a) to narrowest (d). Arrows are barotropic flux vectors. Note how the along-slope barotropic flux is almost entirely confined to conversion dipoles along slope.